Energy Materials

Supplementary Material

Enhancement of Li intercalation kinetics of $LiFePO_4$ nanoparticles with mesoporous carbon

Shaoxin Wei[1], Chaojie Cui[1,2,*], Ying Jin[1], Jin Wang[1], Jian Wang[1], Dongliang Li[2], Weizhong Qian [1,2,*]

[1]Department of Chemical Engineering, Tsinghua University, Beijing 100084, China.

[2]Ordos Laboratory, Ordos 017000, Inner Mongolia, China.

***Correspondence to:** Dr. Chaojie Cui, Department of Chemical Engineering, Tsinghua University, 30 Shuangqing Road, Haidian District, Beijing 100084, China. E-mail: cuicj06@tsinghua.edu.cn; Prof. Weizhong Qian, Department of Chemical Engineering, Tsinghua University, 30 Shuangqing Road, Haidian District, Beijing 100084, China. E-mail: qianwz@tsinghua.edu.cn.

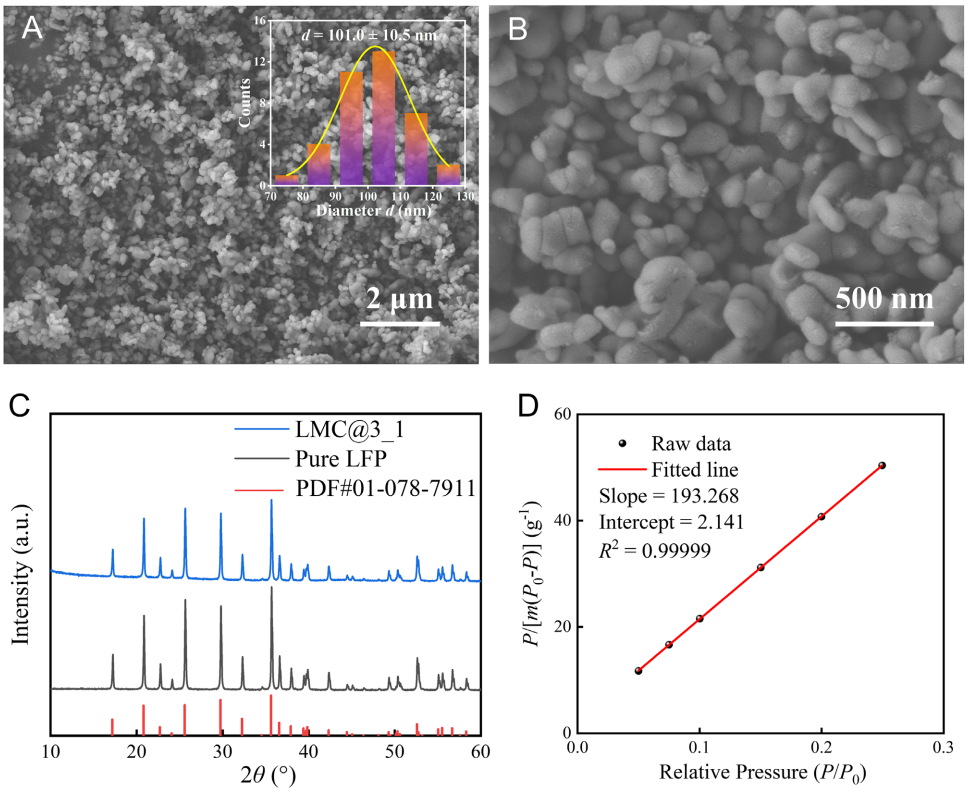

Supplementary Figure 1. Morphology, phase and pore structure characterization of LFP powders. (A–B) SEM images and particle size distribution of nano-sized LFP powders. (C) XRD pattern and the comparison to LMC@3_1 powders and standard XRD pattern (PDF No. 01-078-7911). (D) Multi-point BET linear fitting result.

The LFP spherical particles used in this work exhibited a uniform size distribution with a mean diameter of around 100 nm and a crystal structure with single phase and *Pnma* space group by comparing the standard XRD pattern. LMC@3_1 powders showed a similar XRD pattern with pure LFP powders on account of the amorphous structure of MC. The specific surface area of LFP was 10.955 $m^2 g^{-1}$ according to multi-point BET linear fitting result.

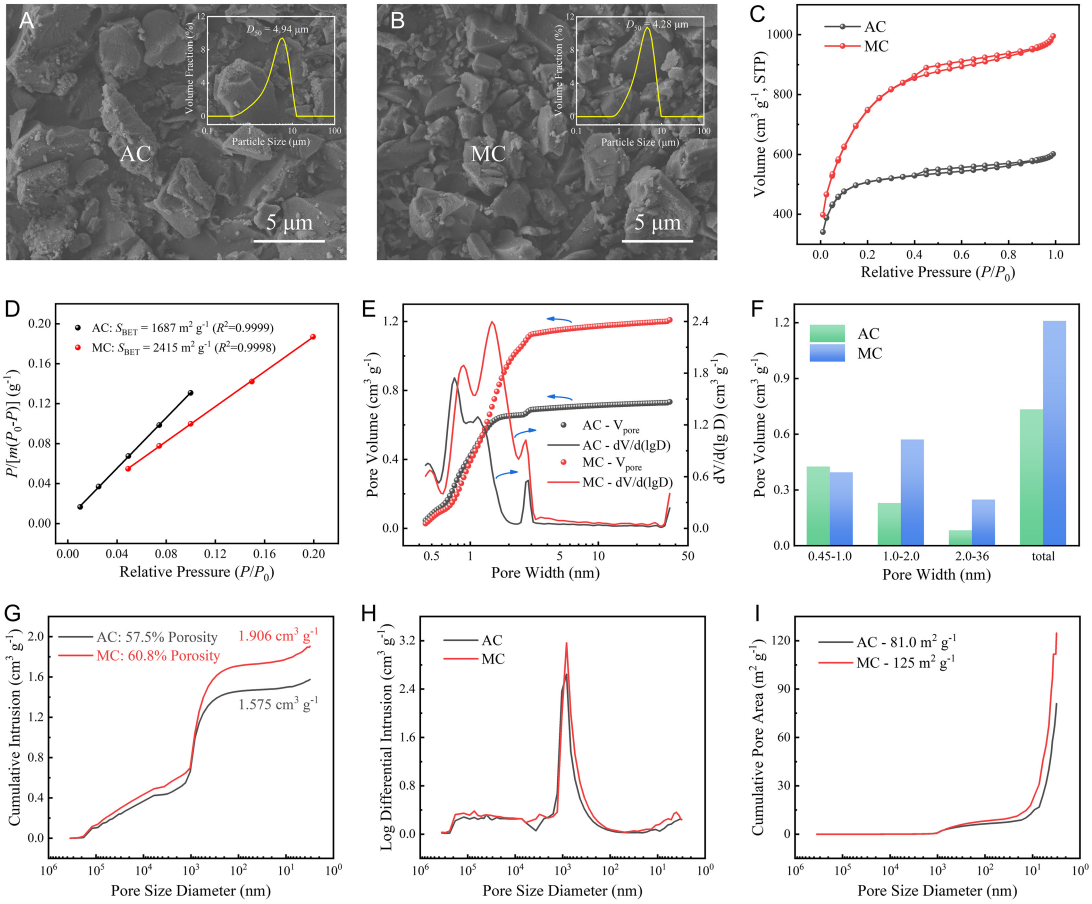

Supplementary Figure 2. Microstructure and pore structure characterization of AC and MC materials. (A–B) SEM image and particle size distribution of: (A) AC powders; (B) MC powders. (C–F) Results of the gas isothermal physical adsorption test for AC and MC powders: (C) Argon sorption isotherms at 87 K; (D) Calculation of specific surface area using BET method; (E) Pore volume and pore size distribution (QSDFT method); (F) Segmented pore volume distribution. (G–I) Results of the mercury intrusion method for AC and MC powders: (G) Cumulative intrusion volume and the porosity; (H) Pore size distribution according to differential intrusion (Log); (I) Cumulative pore area and the total specific surface area within the certain pore range.

MC maintained a similar particle size distribution and porous structure with microporous activated carbon (AC) according to the SEM images. Argon was used as adsorbate instead of nitrogen in this work to avoid the undesired effect between the pore wall and nitrogen molecule resulting from its quadrupole moment. Both AC and MC

exhibited a typical type IV isotherm and a H4 type hysteresis loop at middle P/P_0 region, indicating a capillary condensation during the adsorption/desorption of liquid argon. The BET specific surface area of AC and MC were 1687 and 2415 $m^2\ g^{-1}$. Using QSDFT method, the total pore volume and mesoporous ratio of MC were 1.209 $cm^3\ g^{-1}$ and 20.4%, which of AC were only 0.734 $cm^3\ g^{-1}$ and 11.0%. Mercury intrusion method was further performed to compare the pore distribution larger than 50 nm. It could be seen that the pore content of MC in the range of 2–500 nm was much more abundant than AC, which is conducive to the more electrolyte storage. Owing to sufficient supply of electrolyte and fast transfer path of ions in the large pores, the mesoporous and macro-porous structure of MC would contribute to the capacity retention, stable coulombic efficiency, and stable cycle life.

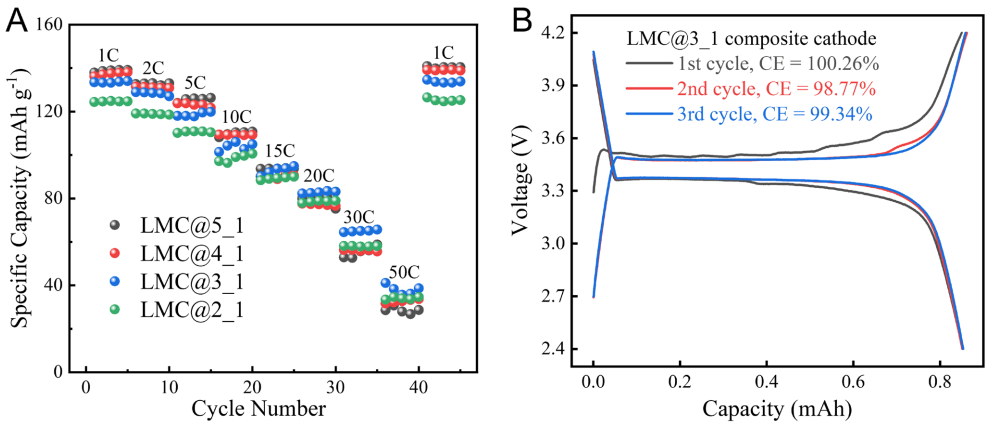

Supplementary Figure 3. (A) Rate performance of LMC cathodes with different mass ratio of MC. (B) Charge-discharge curve and coulomb efficiency (CE) of the first three cycles at 0.2C for LMC@3_1 composite cathode.

Owing to the relatively lower specific capacity of capacitive materials (MC) than battery materials (LFP), a suitable mass ratio of LFP to MC should be carefully researched to achieve the optimal electrochemical performance with both higher capacity and stronger synergistic effect, especially under high discharge rate. Rate performance test of LMC cathodes with different content of MC showed that LMC@3_1 exhibited the highest specific capacity at high discharge rate of 20C–50C, indicating that the most suitable mass ratio of LFP to MC was 3:1 to achieve the best high-power characteristic. In addition, the initial coulomb efficiency (ICE) of LMC@3_1 may be higher than 100% as observed in our test results, indicating the capacity contribution arising from the adsorption of Li-ions in MC in the later stage of the first discharge.

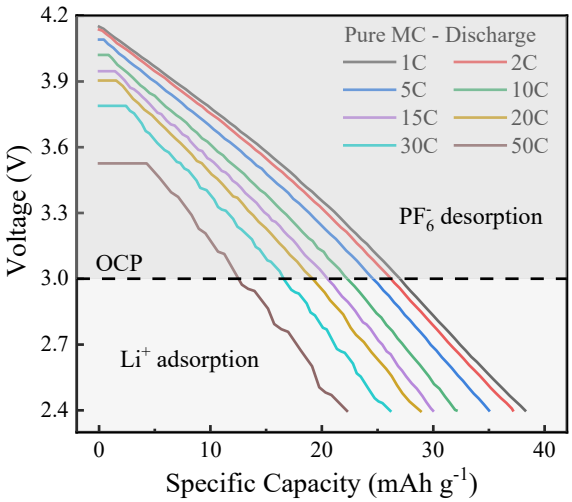

Supplementary Figure 4. Voltage-capacity curves of pure MC cathode at various discharge rates from 1C to 50C.

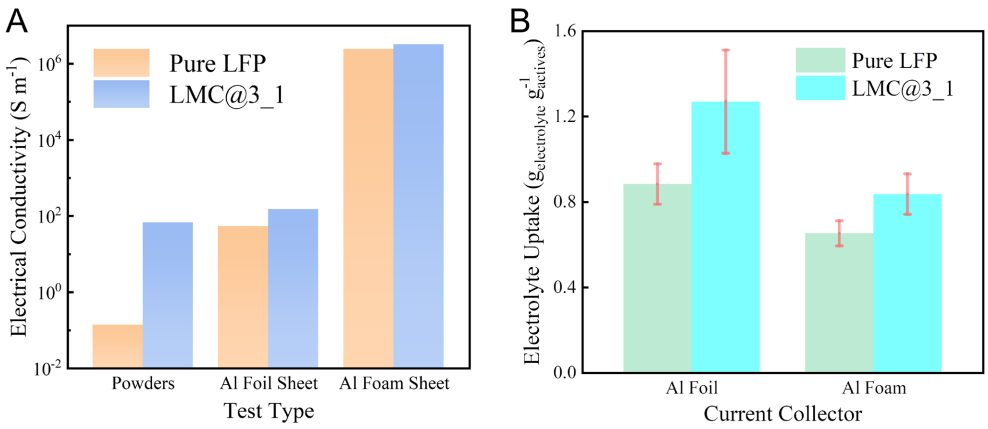

Supplementary Figure 5. (A) Comparison of electrical conductivity between pure LFP and LMC@3_1 cathodes with different test types. (B) Comparison of electrolyte uptake between pure LFP and LMC@3_1 cathodes.

Electrical conductivity was always improved with the addition of MC no matter what test type it was. Moreover, the application of Al foam as current collector had a great increase in electrical conductivity compared to Al foil, proving that Al foam was more conducive to accelerate electron transfer and thus reduce the contact resistance between active materials and current collector. Electrolyte uptake was also improved with the addition of MC. These results indicated that MC could act as auxiliary conductive agent and electrolyte pool to accelerate the transfer of electrons and ions besides providing the capacitive effect.

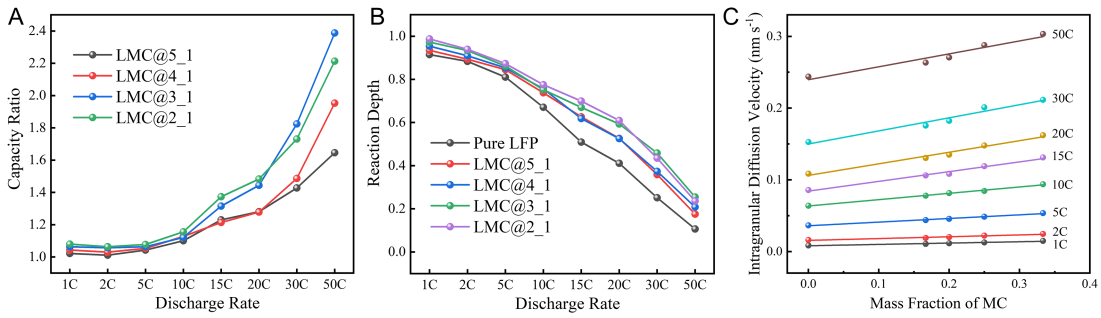

Supplementary Figure 6. Analysis of the synergistic effect between LFP and MC and the Li intercalation kinetics of single LFP particle. (A) Capacity ratio of LMC composite cathodes with different mass ratio of MC under various discharge rates (for pure LFP cathode, CR = 1). (B) Reaction depth of LFP particle in pure LFP and LMC composite cathodes with different mass ratio of MC under various discharge rates. (C) Linear relationship between intragranular diffusion velocity and the mass fraction of MC in LMC composite cathodes under various discharge rates.

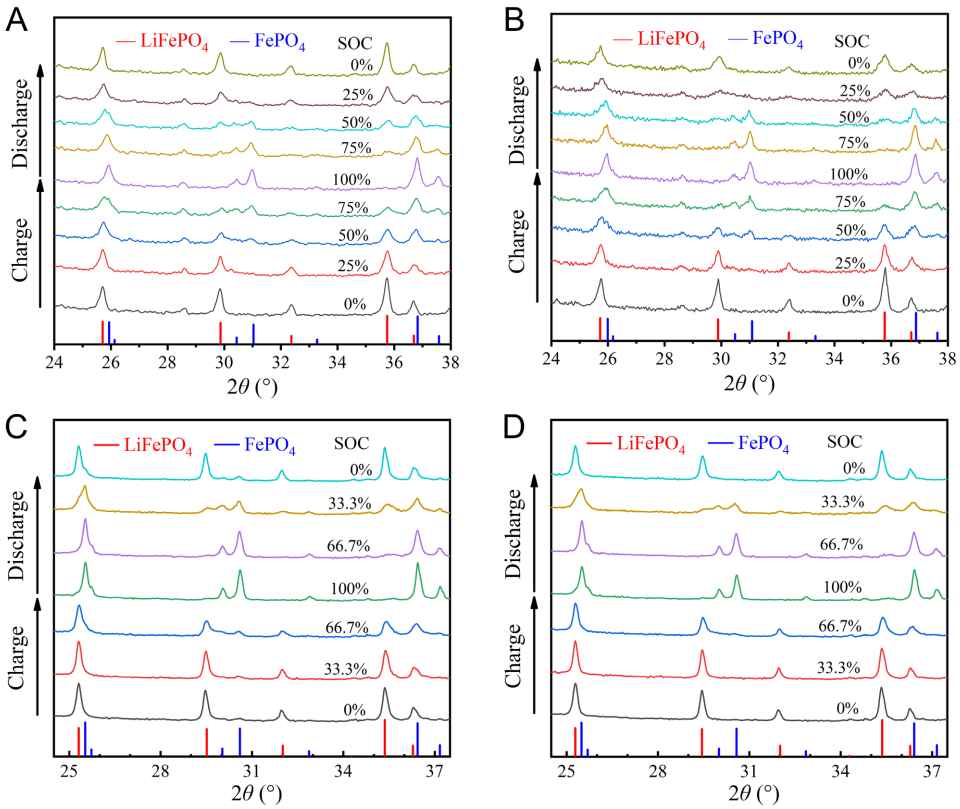

Supplementary Figure 7. A part of original *in-situ* XRD patterns of pure LFP and LMC@3_1 cathodes under two charge/discharge rates. (A) Pure LFP at 0.5C charge/discharge, (B) LMC@3_1 at 0.5C charge/discharge, (C) Pure LFP at 2C charge/discharge, (D) LMC@3_1 at 2C charge/discharge.

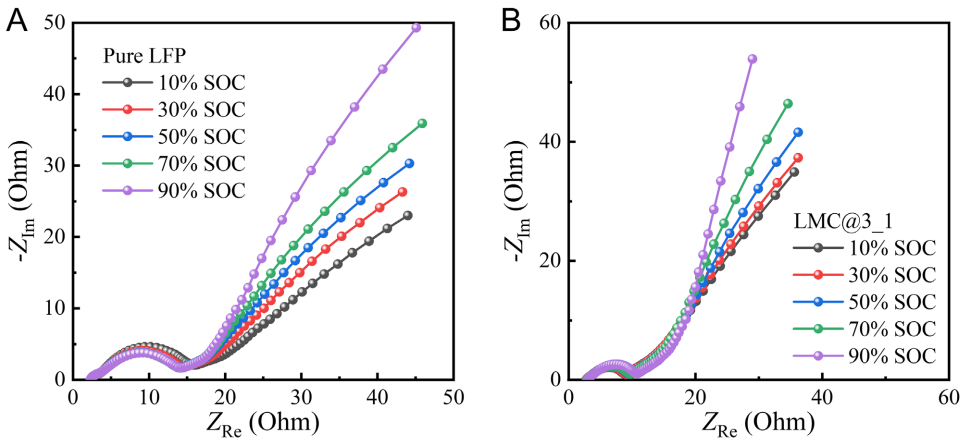

Supplementary Figure 8. Original EIS results at various SOC from 10% to 90%. (A) Pure LFP cathode. (B) LMC@3_1 cathode.

The EIS curves could be divided into four parts and fitted by the equivalent circuit model in Figure 5A in the main text. R_S referred to the ohmic resistance resulting from the resistance of electrolyte, electrodes, and terminals, *etc*. C_{SEI}//R_{SEI} were corresponding to the solid electrolyte interface (SEI) on the LFP or Li metal surface (arc in high-frequency region), while Q_{neg}//R_{neg} were related to the charge transfer process on Li metal/electrolyte interface in the anode (arc in mid-low-frequency region)[1]. More importantly, Q_{dl}//R_{ct} referred to the charge transfer process on the interface of LFP/electrolyte (arc in mid-high-frequency region) and R_{ct} was the charge transfer resistance, representing the difficulty for occurring electrochemical reaction. The linear part in low-frequency region was related to the Li-ion diffusive behavior inside LFP particles and expressed by a constant phase element Q_w in series.

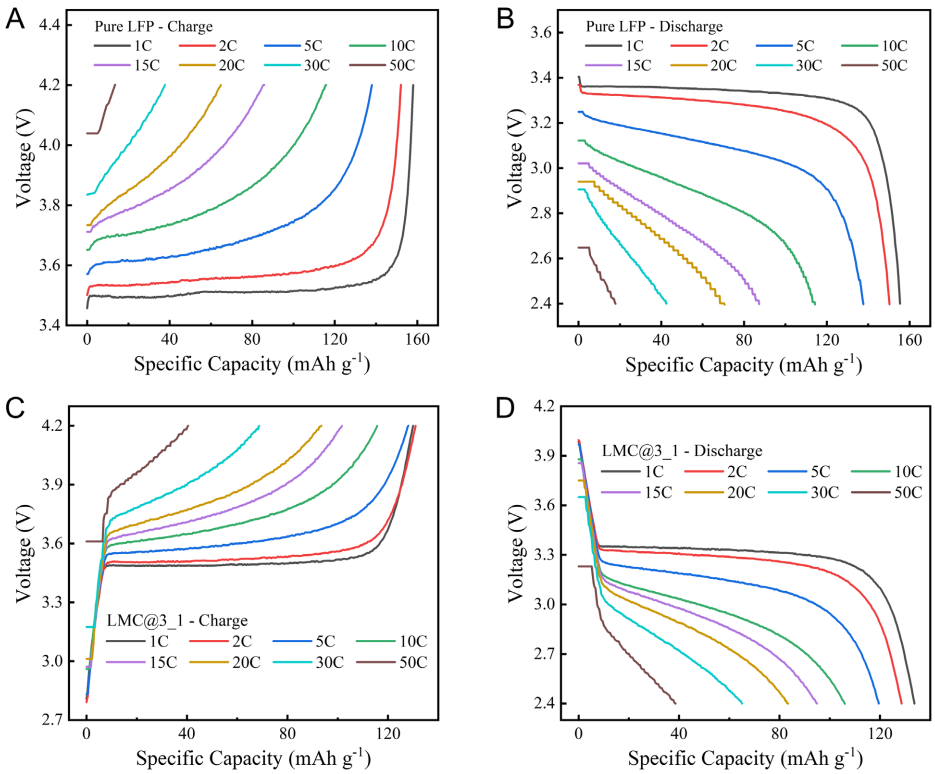

Supplementary Figure 9. Voltage-capacity curves at various rates from 1C to 50C. (A) Pure LFP during charging test. (B) Pure LFP during discharging test. (C) LMC@3_1 during charging test. (D) LMC@3_1 during discharging test.

Supplementary Table 1. Li^+-rich concentration range by MC addition in LMC@3_1 cathode

Current density A g^{-1}	Specific capacity of MC mAh g^{-1}	Specific capacitance of MC (>3.0 V) F g^{-1}	Voltage at inflexion point V	Maximum Li^+-rich concentration mol L^{-1}	Minimum Li^+-rich concentration mol L^{-1}
0.17	38.17	84.55	3.352	0.139	0.051
0.34	37.24	83.22	3.337	0.134	0.048
0.85	35.05	79.69	3.267	0.119	0.037
1.70	32.08	75.62	3.201	0.104	0.026
2.55	30.04	72.43	3.162	0.095	0.020
3.40	28.67	70.28	3.128	0.088	0.015
5.10	26.16	64.50	3.064	0.074	0.007
8.50	22.00	55.63	2.910	0.049	0.000

Supplementary Table 2. C_e and $C_{e,LFP}$ of LMC composite cathodes with different mass ratio of MC under various discharge rates

Rate	C_{LFP}	C_{MC}	LMC@5_1			LMC@4_1			LMC@3_1			LMC@2_1		
			C_e	$C_{e,LFP}$	CC_{MC}	C_e	$C_{e,LFP}$	CC_{MC}	C_e	$C_{e,LFP}$	CC_{MC}	C_e	$C_{e,LFP}$	CC_{MC}
1C	155.50	38.17	138.75	158.87	4.58%	137.37	162.17	5.56%	133.56	165.36	7.14%	124.63	167.86	7.66%
2C	150.15	37.24	132.73	151.83	4.68%	131.14	154.62	5.68%	128.34	158.71	7.25%	118.87	159.69	7.83%
5C	137.78	35.05	125.55	143.65	4.65%	123.09	145.10	5.70%	118.63	146.49	7.39%	110.62	148.41	7.92%
10C	114.01	32.08	109.88	125.44	4.87%	109.24	128.53	5.87%	103.88	127.81	7.72%	98.55	131.79	8.14%
15C	86.59	30.04	93.75	106.49	5.34%	90.09	105.10	6.67%	92.92	113.88	8.08%	89.28	118.90	8.41%
20C	69.86	28.67	79.33	89.46	6.02%	77.17	89.30	7.43%	82.81	100.86	8.66%	78.61	103.58	9.12%
30C	42.73	26.16	55.19	61.00	7.90%	56.04	63.51	9.34%	65.00	77.95	10.06%	58.02	73.95	11.27%
50C	18.12	22.00	28.52	29.82	12.86%	32.71	35.39	13.45%	37.95	43.27	14.49%	34.07	40.11	16.14%

Notes:

(1) The unit of all capacity was mAh g^{-1}.

(2) CC_{MC} meant the capacity contribution of MC (i.e., the anion contribution or the capacitive contribution) in composite cathodes. We assumed the amounts of anions that MC could adsorb/desorb were nearly the same in pure MC cathode and LMC composite cathode, so the CC_{MC} could be calculated by:

$$CC_{MC} = (C_{MC} \times f_{MC})/C_e \times 100\%$$

It could be seen that CC_{MC} increased with the increase of discharge rate and the mass ratio of MC in LMC composite cathode, indicating the better rate performance of MC than LFP.

Supplementary Table 3. The key fitting parameters of EIS results at various SOC

(a) Pure LFP cathode

SOC	R_S Ω	Q_{dl}-Y_0 F s^{n-1}	Q_{dl}-n	R_{ct} Ω	Q_w-Y_0 F s^{n-1}	Q_w-n
10%	2.437	3.5250×10^{-4}	0.8107	11.55	0.10210	0.4593
20%	2.432	3.7568×10^{-4}	0.8021	10.93	0.10444	0.4805
30%	2.427	3.9416×10^{-4}	0.7952	10.54	0.10668	0.5018
40%	2.422	4.0986×10^{-4}	0.7886	10.30	0.10792	0.5243
50%	2.421	4.2648×10^{-4}	0.7821	10.24	0.10827	0.5392
60%	2.421	4.4326×10^{-4}	0.7751	10.26	0.10835	0.5572
70%	2.422	4.6426×10^{-4}	0.7668	10.45	0.10974	0.5847
80%	2.424	4.8100×10^{-4}	0.7605	10.57	0.11249	0.6206
90%	2.423	5.0916×10^{-4}	0.7509	10.89	0.12150	0.6909

(b) LMC@3_1 cathode

SOC	R_S Ω	Q_{dl}-Y_0 F s^{n-1}	Q_{dl}-n	R_{ct} Ω	Q_w-Y_0 F s^{n-1}	Q_w-n
10%	2.925	3.6097×10^{-4}	0.8123	5.475	0.13808	0.6304
20%	2.936	3.6868×10^{-4}	0.8082	5.483	0.13756	0.6344
30%	2.955	3.6967×10^{-4}	0.8055	5.638	0.13921	0.6508
40%	2.974	3.7184×10^{-4}	0.8017	5.890	0.14260	0.6727
50%	2.988	3.7787×10^{-4}	0.7967	6.076	0.14574	0.6928
60%	2.979	3.7134×10^{-4}	0.7978	6.017	0.15065	0.7149
70%	2.993	3.7041×10^{-4}	0.7956	6.190	0.15721	0.7453
80%	3.043	3.6481×10^{-4}	0.7947	6.607	0.16967	0.7910
90%	3.083	3.4100×10^{-4}	0.8018	6.869	0.19621	0.8619

Supplementary Table 4. The electrochemical performance of reported hybrid Li-ion battery-capacitors

Active material composition Cathode // Anode	Voltage V	Specific capacity mAh g^{-1}	Energy density & Power density	Cycle performance	Ref.
75%LFP+5%AC // Li	2.5–4.2	142@0.17A g^{-1} ~ 70@3.4A g^{-1} ^{P}	/	400@100%@1.7A g^{-1} ^{P}	[1]
12%LFP+73%AC // LTO	1.0–2.6	30@0.25C ~ 14@10C	/	100@91%@4C	[2]
34%LFP+51%AC // LTO	1.0–2.6	37@2C ~ 20@10C	/	100@84%@4C	[3]
30%LMO+45%AC // LTO	1.2–2.8	/	16.47Wh kg^{-1}@4C	5000@92%@4C	[4]
65%LFP+20%AC // Li	2.8–4.2	126.2@0.1C ~ 99.4@5C ^{P}	/	500@100%@5C	[5]
65%LFP+20%AC // Li	2.8–4.2	110@0.172A g^{-1} ~ 20@17.2A g^{-1} ^{P}	/	500@98%@8.6A g^{-1} ^{P}	[6]
60%LFP+30%CNT // Li	2.8–4.2	110@0.011A g^{-1} ~ 40@2.27A g^{-1} ^{P}	/	/	[7]
75%NCM+25%AC // Graphite	2.5–4.0	83.5@0.034A g^{-1} ~ 35.2@4.2A g^{-1} ^{P}	294Wh kg^{-1}@100W kg^{-1} 50Wh kg^{-1}@23kW kg^{-1} ^{P}	1000@95%@0.084A g^{-1} ^{P}	[8]
25%NCM+75%AC // HC ^{L}	2.0–4.0	55@0.025A g^{-1} ~ 27@5.0A g^{-1} ^{P}	75.6Wh kg^{-1}@41.7W kg^{-1} 28.5Wh kg^{-1} @6.9kW kg^{-1}	20000@98%@0.5A g^{-1} ^{P}	[9]
67%NCM+33%AC // SC ^{L}	2.5–4.0	92.9@1C ~ 60.9@50C ^{P}	173.3Wh kg^{-1}@26.91W kg^{-1} 92.4Wh kg^{-1}@7.73kW kg^{-1}	10000@80%@10C	[10]
80%LFP+20%AC // LTO	1.0–2.6	96.8@0.1A g^{-1} ~ 57.2@5.0A g^{-1} ^{P}	/	500@93%@1.0A g^{-1} ^{P}	[11]
28%LMO+72%AC // 19%LTO+81%AC	0.5–3.0	49@0.2C ^{P}	53Wh kg^{-1}@100W kg^{-1} 7.3Wh kg^{-1}@27kW kg^{-1}	/	[12]
50%LFP+50%AC // $K_{1.1}Zn_{0.17}Mn_{0.83}F_{3.03}$ ^{L}	0.01–4.3	113@0.1A g^{-1} ~ 68@3.2A g^{-1} ^{P}	81.2Wh kg^{-1}@0.7kW kg^{-1} 9.9Wh kg^{-1}@17kW kg^{-1}	1000@92%@2A/g ^{P}	[13]
75%LFP+25%AC // $KCo_{0.54}Mn_{0.46}F_3$/rGO ^{L}	0–4.4	125@0.1A g^{-1} ~ 73@3.2A g^{-1} ^{P}	229.1Wh kg^{-1}@0.4kW kg^{-1} 78.7Wh kg^{-1}@12.2kW kg^{-1}	1000@89%@1A/g ^{P}	[14]
20%LFP+80%AC // HC ^{L}	2.2–3.8	58.4@0.5C ~ 30@60C ^{P}	30Wh kg^{-1}@5W kg^{-1} 5.7Wh kg^{-1}@2kW kg^{-1} ^{F}	30000@90%@60C	[15]
25%NCM+75%AC // HC ^{L}	2.2–3.8	62.4@0.7C ~ 26.8@36C ^{P}	20Wh kg^{-1}@0.7C ^{F}	20000@90%@18C&36C	[16]
20%LFP+80%AC // HC ^{L}	2.2–3.8	65@7mA g^{-1} ~ 12@7.2A g^{-1} ^{P}	/	100000@92%@60C	[17]
20%LFP+80%AC // HC ^{L}	2.2–3.8	/	21Wh kg^{-1}@10W kg^{-1} 2.8Wh kg^{-1}@5kW kg^{-1} ^{F}	15000@99%@5A	[18]
40%NCM+60%AC // HC ^{L}	2.2–3.8	/	30Wh kg^{-1}@10W kg^{-1} 3.0Wh kg^{-1}@5kW kg^{-1} ^{F}	40000@92%@5A	[19]
30%LFP+70%AC // HC ^{L}	2.2–3.8	75@0.01A g^{-1} ~ 30@3A g^{-1} ^{P}	90Wh kg^{-1}@30W kg^{-1} 30Wh kg^{-1}@3kW kg^{-1}	62000@80%@1.0A g^{-1} ^{P}	[20]
80%LMO+5%AC // 80%LTO+5%AC	1.5–2.7	56.4@0.5C ~ 40.7@5C	60Wh kg^{-1}@5W kg^{-1} 30Wh kg^{-1}@2.5kW kg^{-1} ^{F}	2000@77.5%@5C	[21]
67%LFP+33%PB-AC850 // Li	2.7–4.2	130@0.2C ~ 88.2@10C ^{P}	200Wh kg^{-1}@100W kg^{-1} 90Wh kg^{-1}@10kW kg^{-1} ^{P}	500@93.4%@5C	[22]
77%NCM+3%CA // Li	2.5–4.2	163.8@0.036A g^{-1} ~ 126.8@1.8A g^{-1} ^{P}	/	300@72.79%@0.18A g^{-1}	[23]
80%NCM+5%AC // Graphite	2.8–4.25	150@0.018 A/g ~ 71.8@1.44 A/g ^{P}	/	100@78.46%@0.18 A/g ^{P}	[24]
20%LFP+80%AC // LTO	1.0–2.5	75@0.02A/g ~ 45@8A/g ^{P}	90 Wh kg^{-1}@15W/kg 45 Wh kg^{-1}@15kW/kg	2000@75%@1A/g ^{P}	[25]
75%LFP+25%MC // Li	2.4–4.2	133.6@0.17A g^{-1} 82.8@3.4A g^{-1} 38.0@8.5A g^{-1} ^{P}	437.4Wh kg^{-1}@568.5W kg^{-1} 239.2Wh kg^{-1}@9.8kW kg^{-1} 104.5Wh kg^{-1}@23.4kW kg^{-1} ^{P}	1000@100%@1.7A g^{-1} ^{P}	This work

Notes: (1) Superscript “L” meant the anode had been processed with pre-lithiation before electrochemical test. (2) Superscript “P” meant the data was calculated based on the total mass of active materials in the cathode, Superscript “F” meant the data was calculated based on the total mass of full-cell device and other data was calculated based on the total mass of active materials both in the cathode and anode. (3) “*n*C” meant the discharge process was completed within 1/*n* hour.

Supplementary Calculation 1. Li^+-rich concentration by MC addition

Assuming the specific capacitance of MC adsorbing/desorbing PF_6^- was the same in pure MC cathode and LMC@3_1 cathode, we can derive the Li^+-rich concentration by MC addition in LMC@3_1 cathode according to the specific capacity of MC in pure MC cathode at various current densities as follows.

For pure MC cathode, the OCP was around 3.0 V *vs*. Li/Li^+ and the whole voltage range was 2.4–4.2 V, so the adsorption/desorption of PF_6^- and Li^+ occurred in 3.0–4.2 V and 2.4–3.0 V, respectively (Supplementary Figure 4)[26]. Considering the higher capacitance of PF_6^- adsorption/desorption in porous carbon than that of Li^+[27], we calculated the specific capacitance of MC according to the voltage-capacity curve higher than 3.0 V (corresponding to the adsorption/desorption of PF_6^-). Taking discharge at 1C (equaled to 0.17 A g^{-1}) as an example, the initial voltage was 4.150 V and the specific capacity was 27.01 mAh g^{-1} when the voltage decreased to 3.0 V, so the specific capacitance of MC at 1C could be determined as:

$$27.01 \div (4.150 - 3.0) \times 3.6 = 84.55 \text{ F g}^{-1}$$

According to the charge conservation, we considered that there were *x* mol PF_6^- anions adsorbed at the pore surface of MC if *x* mol electrons passing through the circuit in pure MC cathode, thus generating *x* mol free Li-ions in the electrolyte.

For LMC@3_1, the discharge curve in Figure 1C in the main text showed the voltage at inflexion point was 3.352 V. Since the adsorption and desorption of PF_6^- in LMC@3_1 could occur both in the whole range higher than OCP and in some range lower than OCP, we could firstly obtain the maximum Li^+-rich mole number (based on the mass of MC) at the inflexion point when considering the adsorption/desorption of PF_6^- occurring in the entire voltage range:

$$84.55 \times (3.352 - 2.4) \div 96485 = 8.342 \times 10^{-4} \text{ mol g}^{-1}$$

For LMC@3_1 electrode, the load density of active materials (LFP and MC) and the mass fraction of MC were 0.371 g cm^{-3} and 25%, and the porosity of electrode was 55.8% according to the mercury intrusion method. Assuming that the pores in the

electrode was filled with electrolyte, then the Li^+-rich concentration in LMC@3_1 electrode could be determined as:

$$8.342 \times 10^{-4} \times 0.371 \times 25\% \div 55.8\% \times 10^3 = 0.139 \text{ mol } L^{-1}$$

If considering the adsorption/desorption of PF_6^- only occurring in the range of 3.0–4.2 V, then the minimum Li^+-rich concentration in LMC@3_1 electrode could be determined as:

$$84.55 \times (3.352 - 3.0) \div 96485 \times 0.371 \times 25\% \div 55.8\% \times 10^3 = 0.051 \text{ mol } L^{-1}$$

The actual Li^+-rich concentration in LMC@3_1 electrode should be somewhere between the above maximum and minimum values. The Li^+-rich concentration and relevant data at other current densities were listed in Supplementary Table 1. The specific capacitance of MC and the voltage at inflexion point were acquired from Supplementary Figure 4 and Supplementary Figure 9D.

Supplementary Calculation 2. Li-ion diffusion coefficient according to EIS tests

The linear part in low-frequency region of EIS result is related to the Li-ion diffusion behavior and the corresponding solid-phase Li-ion diffusion coefficient (D_{Li^+}, $cm^2\ s^{-1}$) could be calculated by the following equation[28]:

$$D_{Li^+} = \frac{R^2T^2}{2n^4F^4A^2C_0{}^2\sigma_w{}^2} \qquad \text{Equation (S1)}$$

Here, R is the gas constant (8.314 J mol^{-1} K^{-1}), T is the absolute temperature (K), n is the electron transfer number (n = 1 for LFP), F is the Faraday constant (96485 C mol^{-1}), A is the active area involved in electrochemical reaction and calculated by multiplying the specific surface area of LFP and its mass in the cathode (cm^2), C_0 is the Li-ion molar concentration in the active material ($C_0 = 7.69\times10^{-3}$ mol cm^{-3} for LFP)[28], σ_w is the Warburg factor ($\Omega\ s^{-0.5}$), which equals to the slope of the linear fitting of Z_{Re} to $\omega^{-0.5}$ in low-frequency region (0.01–0.1 Hz in this work), as shown in the inset of Figure 5A in the main text.

References

1. Wang B, Wang Q, Xu B, Liu T, Wang D, Zhao G. The synergy effect on Li storage of LiFePO4 with activated carbon modifications. *RSC Adv* 2013;3:20024-33. [10.1039/c3ra44218g]
2. Hu X, Huai Y, Lin Z, Suo J, Deng Z. A (LiFePO4-AC)/Li4Ti5O12 hybrid battery capacitor. *J Electrochem Soc* 2007;154:1026-30. [10.1149/1.2779947]
3. Hu X, Lin Z, Liu L, Huai Y, Deng Z. Effects of the LiFePO4 content and the preparation method on the properties of (LiFePO4+AC)/Li4Ti5O12 hybrid battery capacitors. *J Serb Chem Soc* 2010;75:1259-69. [10.2298/jsc091228105h]
4. Hu X, Deng Z, Suo J, Pan Z. A high rate, high capacity and long life (LiMn2O4 + AC)/Li4Ti5O12 hybrid battery-supercapacitor. *J Power Sources* 2009;187:635-9. [10.1016/j.jpowsour.2008.11.033]
5. Boeckenfeld N, Kuehnel RS, Passerini S, Winter M, Balducci A. Composite LiFePO4/AC high rate performance electrodes for Li-ion capacitors. *J Power Sources* 2011;196:4136-42. [10.1016/j.jpowsour.2010.11.042]
6. Boeckenfeld N, Placke T, Winter M, Passerini S, Balducci A. The influence of activated carbon on the performance of lithium iron phosphate based electrodes. *Electrochim Acta* 2012;76:130-6. [10.1016/j.electacta.2012.04.152]
7. Varzi A, Ramirez-Castro C, Balducci A, Passerini S. Performance and kinetics of LiFePO4-carbon bi-material electrodes for hybrid devices: A comparative study between activated carbon and multi-walled carbon nanotubes. *J Power Sources* 2015;273:1016-22. [10.1016/j.jpowsour.2014.09.180]
8. Sun X, Zhang X, Huang B, Zhang H, Zhang D, Ma Y. (LiNi0.5Co0.2Mn0.3O2 + AC)/graphite hybrid energy storage device with high specific energy and high rate capability. *J Power Sources* 2013;243:361-8. [10.1016/j.jpowsour.2013.06.038]
9. Sun X, Zhang X, Zhang H, Xu N, Wang K, Ma Y. High performance lithium-ion hybrid capacitors with pre-lithiated hard carbon anodes and bifunctional cathode electrodes. *J Power Sources* 2014;270:318-25. [10.1016/j.jpowsour.2014.07.146]
10. Du T, Liu Z, Sun X et al. Segmented bi-material cathodes to boost the lithium-ion battery-capacitors. *J Power Sources* 2020;478:228994. [10.1016/j.jpowsour.2020.228994]
11. Chen S, Hu H, Wang C, Wang G, Yin J, Cao D. (LiFePO4-AC)/Li4Ti5O12 hybrid supercapacitor: The effect of LiFePO4 content on its performance. *J Renew Sustain Energy* 2012;4:033114. [10.1063/1.4727929]
12. Cericola D, Novak P, Wokaun A, Koetz R. Hybridization of electrochemical capacitors and rechargeable batteries: An experimental analysis of the different possible approaches utilizing activated carbon, Li4Ti5O12 and LiMn2O4. *J Power Sources* 2011;196:10305-13. [10.1016/j.jpowsour.2011.07.032]
13. Ying D, Xu Q, Ding R et al. Insight into pseudocapacitive-diffusion mixed kinetics and conversion-alloying hybrid mechanisms of low-cost Zn-Mn

perovskite fluorides anodes for powerful Li-ion/dual-ion storage. *Chem Eng J* 2020;388:124154. [10.1016/j.cej.2020.124154]

14. Ying D, Ding R, Huang Y et al. Conversion pseudocapacitance-contributing and robust hetero-nanostructural perovskite KCo0.54Mn0.46F3 nanocrystals anchored on graphene nanosheet anodes for advanced lithium-ion capacitors, batteries and their hybrids. *J Mater Chem A* 2019;7:18257-66. [10.1039/c9ta06438a]
15. Jin L, Zheng J, Wu Q et al. Exploiting a hybrid lithium ion power source with a high energy density over 30 Wh/kg. *Mater Today Energy* 2018;7:51-7. [10.1016/j.mtener.2017.12.003]
16. Hagen M, Cao WJ, Shellikeri A et al. Improving the specific energy of Li-Ion capacitor laminate cell using hybrid activated Carbon/LiNi0.5Co0.2Mn0.3O2 as positive electrodes. *J Power Sources* 2018;379:212-8. [10.1016/j.jpowsour.2018.01.036]
17. Shellikeri A, Yturriaga S, Zheng JS et al. Hybrid lithium-ion capacitor with LiFePO4/AC composite cathode - Long term cycle life study, rate effect and charge sharing analysis. *J Power Sources* 2018;392:285-95. [10.1016/j.jpowsour.2018.05.002]
18. Yan J, Chen XJ, Shellikeri A et al. Influence of Lithium Iron Phosphate Positive Electrode Material to Hybrid Lithium-Ion Battery Capacitor (H-LIBC) Energy Storage Devices. *J Electrochem Soc* 2018;165:A2774-A80. [10.1149/2.0911811jes]
19. Hagen M, Yan J, Cao WJ et al. Hybrid lithium-ion battery-capacitor energy storage device with hybrid composite cathode based on activated carbon / LiNi0.5Co0.2Mn0.3O2. *J Power Sources* 2019;433:126689. [10.1016/j.jpowsour.2019.05.095]
20. Guo X, Gong R, Qin N et al. The influence of electrode matching on capacity decaying of hybrid lithium ion capacitor. *J Electroanal Chem* 2019;845:84-91. [10.1016/j.jelechem.2019.05.046]
21. Ruan D, Huang Y, Li L, Yuan J, Qiao Z. A Li4Ti5O12+AC/LiMn2O4+AC hybrid battery capacitor with good cycle performance. *J Alloys Compd* 2017;695:1685-90. [10.1016/j.jallcom.2016.10.318]
22. Peng J, Yu J, Meng B et al. Hierarchical porous biomass activated carbon for hybrid battery capacitors derived from persimmon branches. *Mater Express* 2020;10:523-30. [10.1166/mex.2020.1663]
23. Chen X, Mu Y, Cao G et al. Structure-activity relationship of carbon additives in cathodes for advanced capacitor batteries. *Electrochim Acta* 2022;413:140165. [10.1016/j.electacta.2022.140165]
24. Han Y-L, Wang Z-F, Xie L-J et al. Revealing the accelerated reaction kinetic of Ni-rich cathodes by activated carbons for high performance lithium-ion batteries. *Carbon* 2023;203:445-54. [10.1016/j.carbon.2022.11.077]
25. Lee SH, Huang C, Grant PS. High energy lithium ion capacitors using hybrid

cathodes comprising electrical double layer and intercalation host multi-layers. *Energy Storage Mater* 2020;33:408-15. [10.1016/j.ensm.2020.08.022]

26. Shellikeri A, Hung I, Gan Z, Zheng J. In Situ NMR Tracks Real-Time Li Ion Movement in Hybrid Supercapacitor-Battery Device. *J Phys Chem C* 2016;120:6314-23. [10.1021/acs.jpcc.5b11912]
27. Stepien D, Zhao Z, Dsoke S. Shift to Post-Li-Ion Capacitors: Electrochemical Behavior of Activated Carbon Electrodes in Li-, Na- and K-Salt Containing Organic Electrolytes. *J Electrochem Soc* 2018;165:A2807-A14. [10.1149/2.0921811jes]
28. Fan J, Chen J, Chen Y et al. Hierarchical structure LiFePO4@C synthesized by oleylamine-mediated method for low temperature applications. *J Mater Chem A* 2014;2:4870-3. [10.1039/c3ta15210c]